https://doi.org/10.5194/egusphere-2026-5005
Preprint. Discussion started: 2 September 2026

High altitude precipitation dynamics using long-term observations in a Himalayan catchment

Aris Kwadijk[1], Philip D.A. Kraaijenbrink[1], Faezeh M. Nick[1], Joseph M. Shea[3], Jakob F. Steiner[2,4], René R. Wijngaard[1], and Walter W. Immerzeel[1]

[1]Department of Physical Geography, University of Utrecht, Utrecht, Netherlands
[3]Department of Geography, Earth and Environmental Sciences,University of Northern British Columbia, Prince George, Canada
[2]Department of Geography and Regional Science, University of Graz, Graz, Austria
[4]Asian Mountain Academic Alliance, Kathmandu, Nepal

Correspondence: Aris Kwadijk (a.kwadijk@uu.nl) and Walter W. Immerzeel (w.w.immerzeel@uu.nl)

Abstract. In the Himalayas, the interaction between climate, orography and land cover results in a highly heterogeneous precipitation pattern. Mountain precipitation, being the main driver of the water cycle, ultimately provides water for millions of people downstream. Our current understanding of precipitation patterns within the Himalaya region is mainly based on past modeling efforts and data ensemble products. Yet due to computational limitations these products either cover only a limited time period or are unable to capture fine-scale precipitation patterns due to their resolution. Furthermore, the lack of long-term meteorological observations due to the remoteness and inaccessibility of the terrain results in poor validation of these products, especially above 3000 m a.s.l. We address this knowledge gap by synthesizing thirteen years (2012–2025) of meteorological field data that spans an altitude range between 1406 and 5350 m a.s.l. in the monsoon-dominated Langtang Valley, Nepal. We show that: (i) the diurnal precipitation cycle is bimodal during the monsoon, with an afternoon and a nocturnal peak, but unimodal during the pre-monsoon; (ii) the relative amplitude of the afternoon (nocturnal) peak increases (decreases) linearly with elevation, such that the monsoon precipitation–elevation gradient reverses diurnally from positive in the afternoon to negative at night; and (iii) the nocturnal precipitation, which dominates the monsoon totals, is highly sensitive to valley topography: under the near-saturated conditions prevailing at night, condensation rates scale directly with terrain-forced ascent, concentrating the nocturnal maximum at the steep, confined valley entrance. This elevation gradient of the diurnal cycle offers a simple validation tool for testing whether models capture the topography–circulation interaction, and the observational record provides a unique reference dataset for studying valley-scale precipitation dynamics in this region.

1 Introduction

The Himalayas form one of the worlds most important water towers. Rivers that originate in the Himalayas sustain hundreds of millions of people across downstream river basins (Immerzeel et al., 2019). These rivers are ultimately fed by mountain precipitation, which sustains stream flow both directly, through rainfall and its runoff, and indirectly, through glaciers and snowpacks that release meltwater outside the monsoon (de Kok et al., 2020; Bhattacharya et al., 2021; Pokhrel et al., 2026).

At the same time, extreme precipitation events are a key trigger for natural hazards in the region. Floods and mass movement disasters account for the majority of associated casualties and economic losses (Mal et al., 2018). Understanding precipitation patterns is therefore key for ensuring water security, supporting risk adaptation and improving estimates of glacier mass loss.

Precipitation patterns across the Himalayas are complex, as topography and atmospheric processes interact across multiple spatial and temporal scales (Barros et al., 2004). At the synoptic scale (hundreds of kilometers), the regional climate is defined by a strong seasonal cycle (Yang et al., 2018). In the Central and Eastern Himalayas, the Indian monsoon provides more than 80% of the annual precipitation (Bookhagen and Burbank, 2010). During this period, a low pressure system resides over the Indo-Gangetic Plain and moisture from the Bay of Bengal and the Arabian Sea is transported over the plains. As it moves inland, it traverses over the Bangladesh wetlands and Gangetic Plain region, where it undergoes continued moisture uptake and recycling (Zhou et al., 2017; Hassenruck-Gudipati et al., 2023). Once it reaches the foothills of the Himalayas, the flow is uplifted, where it precipitates mainly at the southern slopes of the Himalayas. These broad seasonal patterns are further organized locally, where valley circulations interact with synoptic-scale weather systems (Bookhagen and Burbank, 2006). The interaction of valley circulations with the synoptic-scale monsoonal jet produces elevation-dependent changes in precipitation timing and amounts during the monsoon (Barros et al., 2004). In the lower elevation (below 2500 m a.s.l.) foothill regions on the southern slopes of the Himalayas, a nocturnal precipitation peak prevails, whereas regions above 3000 m a.s.l. experience a bimodal precipitation pattern with a convective afternoon maximum and a nocturnal maximum (Barros et al., 2000; Sugimoto et al., 2021; Fujinami et al., 2021). The resultant heterogeneous precipitation pattern (Immerzeel et al., 2014) makes precipitation the primary source of uncertainty for glacio-hydrological modeling in the Himalayas (Wang et al., 2024).

Our current understanding of precipitation patterns within the Himalayas also relies on gridded datasets and data ensemble products. Coarse gridded global reanalysis products such as ERA5 or gauge-based products like APHRODITE (both at 0.25°, $\sim$28 km) are geographically complete but are too coarse to incorporate the steep topography, leading to dry biases and an inability to accurately resolve elevation-dependent variables (Yoon et al., 2019). More refined products like ERA5-Land and the High Asia Reanalysis (HAR/HARv2) have been dynamically downscaled to finer resolutions (9 and 10 km) (Wang et al., 2021; Muñoz-Sabater et al., 2021). These products simulate air temperature well, but struggle with spatially more variable components such as valley winds (Khadka et al., 2022). As a result, they cannot reproduce the interaction between the local valley circulation and synoptic-scale weather systems, which drives the diurnal precipitation cycle during the (pre-)monsoon.

Higher-resolution (800 to 500 m) dynamic downscaling with the Weather Research Forecast (WRF) model (Collier and Immerzeel, 2015; Bonekamp et al., 2018) is able to resolve synoptic-scale weather patterns and their interaction with local valley winds (Sugimoto et al., 2021) and, as a result, capture the twice-daily precipitation maxima observed at high altitudes. Still, at slightly coarser resolutions (1 km) the model struggles to fully resolve valley-scale heterogeneity in narrow valley systems where the topography is not properly described (Karki et al., 2017; Sugimoto and Takahashi, 2016). Furthermore, computational limitations restrict these simulations to limited time periods of days to one year (Collier and Immerzeel, 2015; Karki et al., 2017; Bonekamp et al., 2018).

A lack of long-term observational meteorological data, mainly due to the remoteness and inaccessibility of the terrain, limits the effective validation of modeling- and ensemble-based products, especially above 3000 m a.s.l. (Yoon et al., 2019), (Sug-

https://doi.org/10.5194/egusphere-2026-5005
Preprint. Discussion started: 2 September 2026

imoto et al., 2021). Consequently, the valley-scale climatological setting and its complex interactions with local circulation patterns remain poorly understood. The climatology of Himalayan valleys is often determined from single meteorological stations (Shea et al., 2015), which are typically located on the valley floors (Bharti and Singh, 2015). For precipitation in particular, such point measurements are often not representative of the catchment as a whole given the high spatial heterogeneity. Relying on sparse valley-bottom data to extrapolate conditions at high altitude glacierized zones adds a major source of uncertainty (Immerzeel et al., 2014). Multi-station networks that have been set up in selected Himalayan catchments, including the Khumbu region through the Pyramid Meteorological Network (EvK2CNR, 2025; Salerno et al., 2025), the Rolwaling (Weidinger et al., 2021) and the Langtang Valley (Immerzeel et al., 2014; Steiner et al., 2021) allow for comparative high altitude analyzes across the region. These networks have substantially contributed to our understanding of valley-scale climatology, but remain few in number and are unevenly distributed across the Himalayas.

This study builds on the existing Langtang Valley network and extends it, both in terms of the number of stations and the length of the observational record. We aim to improve our understanding of precipitation dynamics in the Himalayas through a synthesis of meteorological field data (2012–2025), collected across an altitudinal range of 1406–5350 m a.s.l. by a dense network of meteorological stations located inside the valley. This dataset is unique due to the rare combination of its long-term measurement period and high density of stations within a single valley. Based solely on observed ground data, we aim to (i) document the spatial heterogeneity within the valley, (ii) provide a quantitative climatological benchmark for hourly to monthly timescales across the full altitudinal range, and (iii) investigate how the interaction between the synoptic setting and local topography drives the heterogeneous precipitation patterns inside the valley. Findings of this study may serve as a reference dataset to validate how larger-scale modeling and satellite products resolve valley-scale meteorological processes.

2 Study Area

Langtang Valley is situated in central Nepal (28.2°N, 85.5°(e) and covers an area of 585 km^2, spanning from 1400 m a.s.l. up to 7234 m a.s.l. (Fig. 1). The Langtang River is the headwater of the Trishuli River in the Narayani (Gandaki) River system, one of the major trans-Himalayan river systems that drains into the Ganges. Approximately 25% of the area is glacierized (Steiner et al., 2021). The relative contributions of rainfall and snowmelt to streamflow vary considerably across seasons. During the pre-monsoon, rainfall and snowmelt contribute roughly equally to total discharge, whereas the monsoon is dominated by rainfall. In the winter and post-monsoon periods, discharge drops markedly as both rainfall and snowmelt diminish (Immerzeel et al., 2014).

From the valley entrance at Syabru Besi (1406 m a.s.l.) to Ghoda Tabela (3040 m a.s.l.), the valley is characterized by a steep, river-incised V-shape (Fig. 1b). Above Ghoda Tabela, the valley transforms into a glacially carved U-shape with gentler slopes and a flat valley bottom (Fig. 1c).

In the study area, 70–90 % of total annual precipitation is delivered during the Indian monsoon (Immerzeel et al., 2014). Regional daily precipitation quantities correlate with the strength of the lower level meridional winds along the slopes of the valley and south of the catchment (Collier and Immerzeel, 2015). At the end of the monsoon and the beginning of the

https://doi.org/10.5194/egusphere-2026-5005
Preprint. Discussion started: 2 September 2026

post monsoon, cyclonic storms occur. During these events, 3–6 day synoptic scale low pressure systems, developed over and around the Bay of Bengal are diverted towards the Himalayas (Fujinami et al., 2021). These systems advect large amounts of moisture that, when forced over steep terrain, result in high daily precipitation totals in the valley. During winter, precipitation is governed by synoptic disturbances from the Mediterranean and Caspian Sea and has a more stratiform character (Cannon et al., 2016).

A heterogeneous precipitation pattern exists inside the Langtang Valley (Immerzeel et al., 2014; Ueno et al., 1993). Previous modeling efforts showed that during the monsoon, precipitation accumulates mainly at lower elevations with drying conditions further up the valley. In winter, precipitation peaks at an altitude of 5000–6000 m a.s.l. (Collier and Immerzeel, 2015). Four seasons are defined for this study: pre-monsoon (March to June 15), monsoon (June 15 to September), post-monsoon (October to December), and winter (January to February). The seasons are determined by the onset and termination of the monsoonal jet, which typically establishes around mid-June (Adhikari et al., 2022).

3 Method

3.1 Meteorological stations

Since 2012, a monitoring network has been installed and incrementally expanded through a collaboration between Utrecht University, the Nepal Department of Hydrology and Meteorology (DHM), Eidgenössische Technische Hochschule Zürich (ETH Zürich) and the International Centre for Integrated Mountain Development (ICIMOD). Stations and meteorological variables selected for this research are quality checked based on their data coverage, outliers and number of valid measurements. Locations of the meteorological stations throughout the valley are indicated in Fig. 1. PLU1, TB1–2, TB6–7 and TB9–10 are located on the main valley bottom. TB8 and PLU4 are situated inside tributary valleys. TB3-5 are located on the slopes south of Kyangjin Village, whereas PLU2 is located near the tongue of Yala Glacier on the northern slopes of Kyangjin Village. Precipitation is measured using weighing pluviometers or tipping buckets. The pluviometers weigh the mass of liquid and solid precipitation that fall in the bucket at 10 or 15 minute interval, and data are subsequently aggregated to hourly intervals. Tipping buckets are event based and record a timestamp after every 0.2 mm of liquid precipitation only. For consistency, the tipping bucket data are also aggregated to hourly totals. Single-Alter windscreens were mounted around each pluviometer to reduce gauge undercatch (Fig. 2b).

Individual pluviometers have been further equipped with (a subset of) sensors that measure air temperature and relative humidity (RH), wind speed, and direction, mean incoming shortwave and longwave radiation ($\mathrm{SW_{in}}/\mathrm{LW_{in}}$) and atmospheric pressure (Table 1). Air temperature and RH sensors are housed in unventilated radiation shields. All data are recorded in local time (UTC+5:45). An overview of the variables measured, instrumentation and specifications is given in Table 1, and by Steiner et al. (2021), who provides a comprehensive description of the full sensor network present in the Langtang Valley.

https://doi.org/10.5194/egusphere-2026-5005
Preprint. Discussion started: 2 September 2026

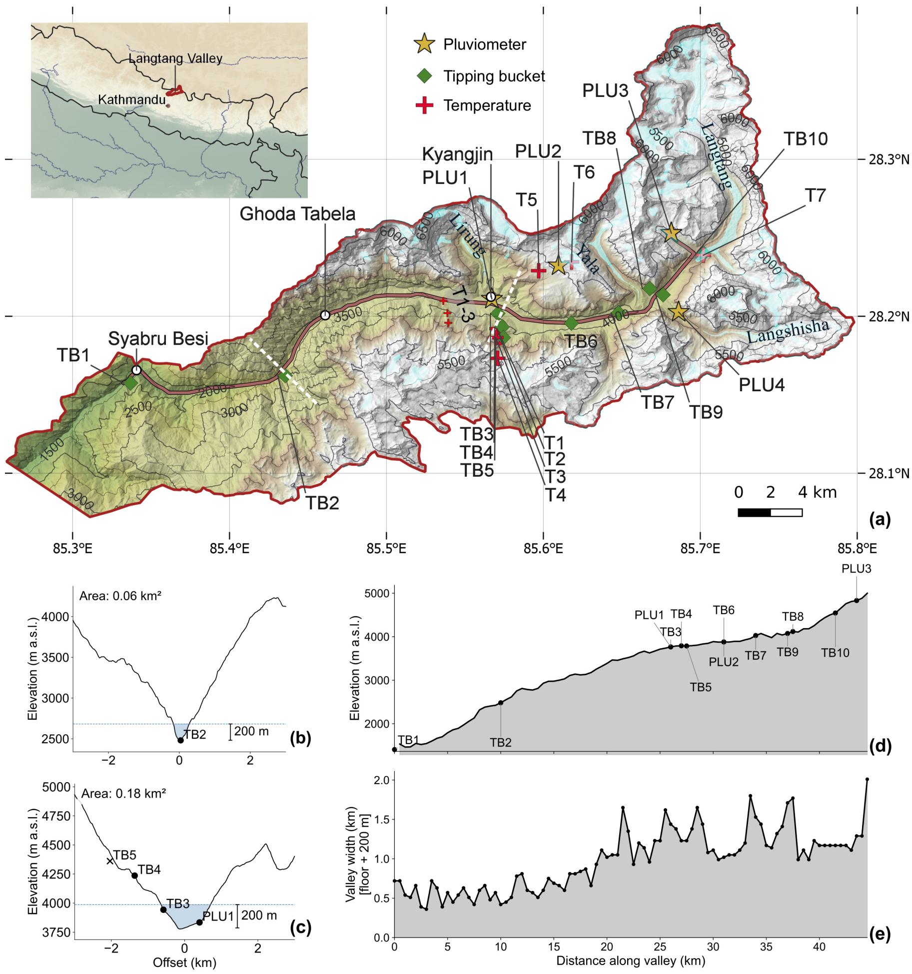

Figure 1. (a) Map of the Langtang Valley indicating the station locations. (b, c) Cross-sections at TB2 and Kyangjin Village (locations indicated by white dotted lines in (a)); the blue dotted line indicates the valley width at +200 m above the valley floor, and blue shading indicates the valley cross-sectional area up to 200 m above the valley floor. (d) Elevation profile along the valley floor, indicated by the orange line in (a). (e) Valley width at +200 m above the valley floor along the valley profile. Sources: Pléiades © CNES 2017,2022, Distribution Airbus D&S; ESRI; SRTM | Powered by Esri

3.2 Data pre-processing

3.2.1 Precipitation phase partitioning

To distinguish between rain and snow, a temperature-based phase threshold of 1 °C was chosen. This threshold falls within the range used by other studies in the region: (0.5 °C; Saloranta et al., 2019), (1 °C; Romshoo et al., 2023), and (< -2 °C for snow, > 2 °C for rain and -2 to 2 °C for mixed precipitation; Kirkham et al., 2019). The sensitivity of changes in snowfall estimates

https://doi.org/10.5194/egusphere-2026-5005
Preprint. Discussion started: 2 September 2026

Table 1. Station details, sensors, and variables monitored. Sensor thresholds and accuracies are listed in Table 2. Measurements are generally taken at approximately 2 m above the surface. Wind sensors at PLU1, 2 and 3 are mounted at 3.3 m, 2.5 m and 1.5 m respectively. Temperature and wind data are directly aggregated to hourly means. Precipitation is aggregated to hourly sums.

Station	Variables	Sampling interval	Sensors
Tipping buckets (TB)			
TB1, 2, 6	rain	0.2 mm	ARG-100
TB3–5, 9	rain, air temperature	0.2 mm / 1, 10, 30 min	Casella; CS215
TB7	rain	0.2 mm	Casella
TB8, 10	rain, air temperature	0.2 mm / 10, 30, 60 min	Casella; CS215
Pluviometers (PLU)			
PLU1	rain, snow, air temperature, RH, wind, atm. pressure, SW_{in}/LW_{in}	10 min	OTT-2; HC2S3; CNR4; PTB330 (pre-2015) $\rightarrow$ CS106 (post-2015)
PLU2	rain, snow, air temperature, RH, wind, atm. pressure, SW_{in}/LW_{in}	10 min	OTT-2; HC2S3; 05103-45-L; CNR4
PLU3	rain, snow, air temperature, RH, wind, atm. pressure	15 min	OTT-2; CS109-L; WS500-UMB
PLU4	rain, snow, air temperature	15 min	OTT-2; HC2S3
Temperature sensors (T)			
T1–2, 4	air temperature	60 min	CS215
T3	air temperature	15 min	—
T5	air temperature	15 min	CS109-L
T6	air temperature	10 min	HC2S3
T7	air temperature	5 min	—

to the choice of commonly used temperature thresholds is illustrated in Fig. A1. For tipping buckets lacking temperature observations, hourly air temperatures are estimated by extrapolating temperature data from PLU1, using linearly interpolated temperature lapse rates. Temperatures measured by TB3–5, TB7 and TB9 are only used to distinguish between snow and rain at the station site, but are excluded from further temperature analysis due to inaccurate temperature measurements at these stations. For tipping buckets, snowfall is not recorded at the time it falls, but rather when it subsequently melts and passes through the tipping mechanism. To avoid misinterpreting these as zero-precipitation measurements, all zero measurements for the tipping buckets below 1 °C are removed from the time-series. Above 4000 m a.s.l. between October and May, temperatures

https://doi.org/10.5194/egusphere-2026-5005
Preprint. Discussion started: 2 September 2026

Table 2. Sensor thresholds and accuracies. ARG, HC, 05103-45-L and sensors abbreviated with CS are distributed by Campbell Scientific; the CNR4 is produced by Kipp & Zonen, the WS500-UMB by Lufft, the PTB330 and CS106 by Vaisala and the OTT-2 by OTT HydroMet, 05103-45-L by R.M. Young, ARG-100 by EML and HC2S3 Rotronic

Sensor	Measures	Threshold / accuracy
ARG-100	rain	0.2 mm / $\pm$ 1 % at 0.5 $\mathrm{m\,h^{-1}}$
Casella	rain	0.2 mm / $\pm$ 2 % at 1 L
OTT-2	rain, snow	0.05 mm / $\pm$ 6 $\mathrm{mm\,h^{-1}}$
CS215	air temperature, RH	$\pm$ 0.4 $^\circ\mathrm{C}$ / $\pm$ 2% at 25 $^\circ\mathrm{C}$ (10–90 % range)
CS109-L	air temperature	$\pm$ 0.2 $^\circ\mathrm{C}$
HC2S3	air temperature, RH	$\pm$ 0.1 $^\circ\mathrm{C}$ / $\pm$ 0.8%
PTB330	atm. pressure	$\pm$ 0.20 hPa at + 20 $^\circ\mathrm{C}$
CS106	atm. pressure	$\pm$ 1.0 hPa / $-$20 to + 45 $^\circ\mathrm{C}$
CNR4	$\mathrm{SW_{in}/LW_{in}}$	< 10%/day / 0 < SW < 2000 $\mathrm{W\,m^{-2}}$
WS500-UMB	wind, RH, atm. pressure	wind: $\pm$ 0.3 $\mathrm{m\,s^{-1}}$ / $\pm$ 3%; dir: <3° RMSE; RH: $\pm$ 0.2%; atm. pressure: $\pm$ 0.5 hPa at 0–40 $^\circ\mathrm{C}$
05103-45-L	wind	1–100 $\mathrm{m\,s^{-1}}$/$\pm$ 0.3 $\mathrm{m\,s^{-1}}$ or 1 %

are frequently below 1 $^\circ\mathrm{C}$ (Fig. A2), making the exact timing of hourly precipitation data for tipping buckets unreliable outside of the monsoon season. We assume that nighttime snowfall during the pre- and post-monsoon is retained in the bucket and melts each morning. Consequently, only daily and monthly totals are used during these seasons. Measurement periods for each station and variable used for further analysis is presented in Fig. 2.

3.2.2 Quality control and data filtering

To ensure data reliability, several quality-control filters were applied. Pluviometer records were screened by removing flagged data and precipitation intensities exceeding 100 $\mathrm{mm\,h^{-1}}$, which is above the reported regional precipitation intensity maximum observed by Bookhagen and Burbank (2010) (40-60 $\mathrm{mm\,h^{-1}}$). In addition, all hourly observations above 40 $\mathrm{mm\,h^{-1}}$ (n = 19) were cross-checked against documented extreme events in Nepal (news reports and literature) and station maintenance records. Observations that could not be corroborated were classified as outliers and discarded. For the tipping-bucket gauges, a stricter threshold of 40 $\mathrm{mm\,h^{-1}}$ was applied, as these stations are not used for extreme-value analysis and the threshold is assumed to have a negligible effect on multi-year monthly and hourly means. Wind speeds of 0 $\mathrm{m\,s^{-1}}$ and above 50 $\mathrm{m\,s^{-1}}$ are removed based on visual inspection of the data. Because multiple refractions from surrounding snow-covered terrain and clouds results in incoming solar radiation frequently exceeding the solar constant, a maximum $\mathrm{SW_{in}}$ of 2000 $\mathrm{W\,m^{-2}}$ was implemented (Gel-

https://doi.org/10.5194/egusphere-2026-5005
Preprint. Discussion started: 2 September 2026

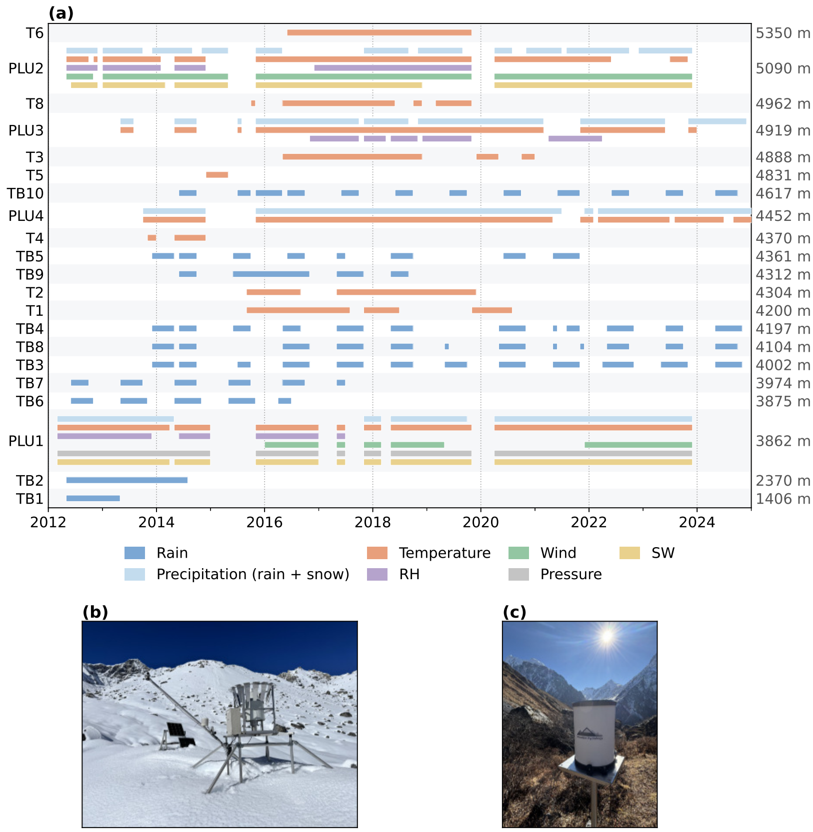

Figure 2. (a) Overview of data availability (after pre-processing) per meteorological variable at each station. TB = tipping bucket; SW = mean incoming shortwave radiation; LW = mean incoming longwave radiation. (b) Pluviometer (PLU3). (c) Casella tipping bucket (TB8).

sor et al., 2021). During winter, snow insulates the temperature sensors at the tipping buckets, dampening diurnal temperature fluctuations. We identified these periods and removed them manually from the dataset. To prevent spillover error, precipitation data from the pluviometer is excluded if the gauge reaches 95 % of its capacity. Precipitation totals are computed for monthly, daily and hourly timescales. Monthly totals were obtained by summing hourly precipitation values recorded by the pluviometers. Because pluviometers continuously measure weight differences, any missing timestamps directly lower the calculated totals. Therefore, we applied strict data coverage thresholds for these instruments, requiring 100 % coverage for monthly and daily totals.

A lower coverage threshold is applied for the tipping buckets to account for the freeze and melt cycles that occur during periods of nighttime snowfall and daytime melting. Aggregated monthly sums are calculated when at least 50 % of the data within a month is valid. Additionally, extended periods of zero precipitation were cross-checked against neighboring stations.

https://doi.org/10.5194/egusphere-2026-5005
Preprint. Discussion started: 2 September 2026

Where a station recorded no precipitation over a prolonged period while nearby stations did, the data were flagged as instrument failure and excluded from the analysis to avoid false zero measurements. Fig. 2 provides an overview of the data used for further analysis.

Monthly precipitation means were computed with at least three months satisfying the coverage thresholds for tipping buckets and pluviometers. TB1 is an exception, as it measures for a single year. This station is still considered valuable as it provides coverage in the lower elevation but its monthly precipitation totals should be treated with caution. Annual totals for pluviometers are produced as the sum of all monthly means.

3.2.3 Wind-induced precipitation undercatch

Undercatch of liquid precipitation for the ARG100 and Casella tipping buckets was quantified on a wind exposed site by Pollock et al. (2018). At wind speeds similar to the Langtang Valley during the monsoon (4–5 $\mathrm{m\,s^{-1}}$), they report a systematic undercatch of 9 % for the Casalla bucket (mounted at 0.5 m above the ground). Under strong winds comparable to winter and post-monsoon precipitation events (10 $\mathrm{m\,s^{-1}}$ on average), undercatch increases to 17 % for the ARG100 (1.5 m) and 24 % for the Casella (0.5 m). Actual undercatch at our sites is likely higher, as the undercatch of solid precipitation, which typically exceeds that of rain, could not be quantified due to the lack of wind measurements at the tipping bucket sites. Since the pluviometers are equipped with windshields, undercatch of liquid precipitation is considered negligible. For mixed and solid precipitation, however, undercatch remains substantial. Therefore, this study applies the correction from Kochendorfer et al. (2017) to account for wind-induced undercatch for mixed and solid precipitation recorded at the pluviometer. Based on their empirical relation, we estimated undercatch of 7, 18, 15 and 32 % for the monsoon, pre-monsoon, post-monsoon and winter respectively (Fig. A3).

3.3 Analysis of atmospheric drivers and precipitation dynamics

To analyze the precipitation dynamics in Langtang Valley, we focus on key metrics derived from the surface observations: $\mathrm{SW_{in}}$ to $\mathrm{LW_{in}}$ ratio (SW/LW), surface temperature lapse rate (LR), zero-degree isotherm ($z_{0^\circ\mathrm{C}}$), and albedo ($\mathrm{SW_{in}}$/$\mathrm{SW_{out}}$).

SW/LW is a measure for the radiative forcing at the surface that drives the thermal valley circulation (Kirshbaum et al., 2018). High SW/LW indicate clear-sky conditions, under which the slopes warm rapidly during the day through direct insolation and cool rapidly at night through longwave emission. Low values are indicative of cloudy conditions, where clouds block $\mathrm{SW_{in}}$ and re-emit $\mathrm{LW_{in}}$, dampening daytime surface heating and nocturnal radiative cooling. The mean monthly $\mathrm{SW_{in}}$ to $\mathrm{LW_{in}}$ ratios are calculated as the daily mean $\mathrm{SW_{in}}$ divided by the daily mean $\mathrm{LW_{in}}$. The daily ratios are subsequently aggregated to monthly mean ratios.

The valley circulation is driven by the horizontal pressure gradients that arise hydrostatically from temperature contrasts between the valley atmosphere and the adjacent air columns (Whiteman and Doran, 1993). Because these temperature contrasts are generated by surface heating along the terrain, the surface lapse rate derived from the station network provides a proxy for the strength of this thermal forcing. A steep LR indicates a strong thermal gradient within the valley that drives buoyant anabatic (upslope) winds in the afternoon and density-driven katabatic (downslope) winds at night. Hourly LR have previously been

https://doi.org/10.5194/egusphere-2026-5005
Preprint. Discussion started: 2 September 2026

determined before in the study area for its use in hydrological modeling (Heynen et al., 2016; Immerzeel et al., 2014; Shea et al., 2015) and are here extended over a longer measurement period.

Here, hourly LRs are determined by fitting a first-order linear regression between station elevation and observed hourly temperatures for at least six stations at every hour. To show how the diurnal wind patterns shift seasonally, wind direction is reduced to upslope and downslope directed based on the local topographic orientation of each wind station.

Atmospheric moisture availability and saturation are quantified as the mixing ratio (MR) and RH at PLU1–3, which vary both in altitude and lateral position inside the valley. MR is calculated using the actual vapor pressure and atmospheric pressure using the Mangus Tetens formulation (Tetens, 1930), with the optimized coefficients as defined by Bolton (1980). RH is directly measured at these stations.

To analyze the elevation of the snowline inside the valley, elevation (z) of the zero-degree isotherm ($z_{0^\circ\mathrm{C}}$) is calculated daily mean temperatures and LR according to

$$z_{0^\circ\mathrm{C}} = -\frac{T_{z=0}}{\Gamma}, \tag{1}$$

where $T_{z=0}$ is the temperature extrapolated to $z = 0$ and Γ is the daily mean LR. The resulting $z_{0^\circ\mathrm{C}}$ is constrained between 0 and 8000 m a.s.l. The presence of a snowpack is independently confirmed using surface albedo. This is quantified as the ratio of outgoing to incoming shortwave radiation ($\mathrm{SW_{out}}/\mathrm{SW_{in}}$; 08:00–18:00, $\mathrm{SW_{in}} > 150\,\mathrm{W\,m^{-2}}$).

Temperature, RH, MR, LR and $z_{0^\circ\mathrm{C}}$ are analyzed on monthly timescales. Available measurements as indicated in Fig. 2, are grouped per month to compute monthly means. Additionally, diurnal cycles for each season are analyzed for temperature, precipitation, LR, RH, MR and wind- speed and direction. To do this, observations are grouped by hour of day and by season/month, from which hourly seasonal/monthly means are computed over a 24-hour window.

To characterize how precipitation is distributed spatially and temporally across the valley during the monsoon, two additional analyses are performed. A Spearman correlation matrix is constructed from hourly precipitation records at all available stations, providing a measure of spatial coherence. Low inter-station correlations are indicative of localized, convective precipitation events, while high correlations point to widespread, stratiform precipitation affecting multiple gauges simultaneously.

Lastly, to formulate a generalized trend of how the monsoon diurnal cycle evolves across the elevational range, hourly monsoonal precipitation is normalized as

$$\hat{p}(s,h) = \frac{\overline{p}(s,h)}{\overline{p}(s)}, \tag{2}$$

where $\overline{p}(s,h)$ is the mean precipitation at specific hour h at station s and $\overline{p}(s)$ is the seasonal hourly mean at station s. A value of $\hat{p} > 1$ indicates that precipitation at that hour exceeds the daily hourly mean, while $\hat{p} < 1$ indicates it falls below. Because normalization removes the station-specific totals imposed by the local micro-climatic setting, it isolates the shape of the diurnal precipitation cycle allowing comparison directly across different stations.

https://doi.org/10.5194/egusphere-2026-5005
Preprint. Discussion started: 2 September 2026

4 Results

4.1 Climatic overview

4.1.1 Thermodynamical drivers and moisture advection

Mean monthly temperatures peak in July, ranging from $+9.8\,°\mathrm{C}$ at PLU1 to $+3.7\,°\mathrm{C}$ at PLU2 (Fig. 3a). The coldest month is January, with mean temperatures between -2.6 and $-10.4\,°\mathrm{C}$ at PLU1 and PLU2, respectively. $z_{0°\mathrm{C}}$ remains consistently above 5500 m a.s.l. during the monsoon (Fig. 3b), resulting in melt across glaciated areas inside the catchment. In October temperatures drop rapidly and $z_{0°\mathrm{C}}$ descends to 3200 m a.s.l. during winter. During the pre-monsoon, $z_{0°\mathrm{C}}$ gradually increases to 4800 m a.s.l., initiating melt in the majority of the catchment.

The pre-monsoon is characterized by steep LR ($-6.9\,°\mathrm{C\,km^{-1}}$) and large diurnal temperature ranges (Fig. 3a,d). The SW/LW ratios and low RH values reflect dry, largely cloud-free conditions (Fig. 3c,f). Under clear sky conditions, solar radiation, unattenuated by clouds, drives intense daytime heating that is most pronounced at higher elevations, due to the thinner atmosphere here. At night, the absence of a cloud layer reduces LW, promoting strong radiative cooling at the surface. This combination of intense daytime surface heating and strong nocturnal radiative cooling results in large diurnal temperature variability.

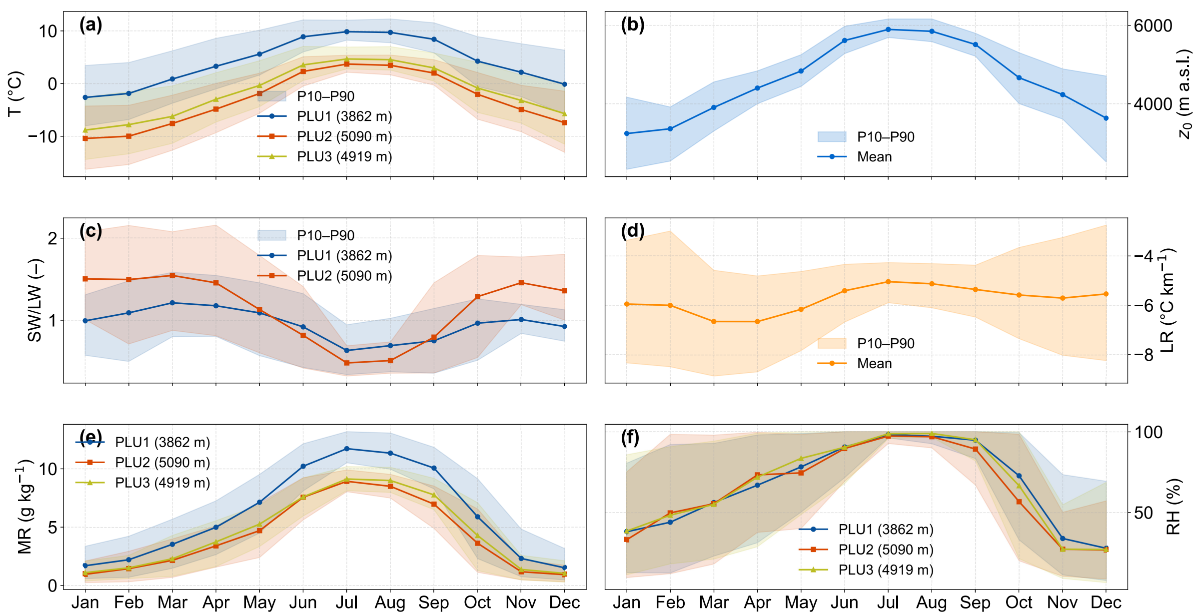

Figure 3. Mean monthly (a) temperature, (b) zero-degree isotherm elevation, (c) SW/LW ratio, (d) temperature LR, (e) mixing ratio and (f) relative humidity.

The monsoon onset is marked by a sharp rise in MR and RH from June onward (Fig. 3e,f), reflecting high moisture advection driven by the monsoonal jet. Mean monthly MR reaches 8–12 $\mathrm{g\,kg^{-1}}$ across the valley. The atmospheric moisture

https://doi.org/10.5194/egusphere-2026-5005
Preprint. Discussion started: 2 September 2026

storage capacity declines with elevation, resulting in lower MR measured at PLU2 and PLU3 (±8 $\mathrm{g\,kg^{-1}}$), compared to PLU1 (± 10 $\mathrm{g\,kg^{-1}}$). Despite this lower absolute moisture content, the colder temperatures at higher elevations keep the air close to saturation, so near-saturated conditions (97–99 %) prevail throughout July and August across all stations. In addition, SW/LW is relatively low due to a persistent cloud cover, particularly at higher elevation (PLU2), where frequent afternoon convective clouds develop at the ridges (Ueno et al., 1993). These humid conditions promote condensation and the associated release of latent heat, which drives an upward transfer of heat and causes a shallowing of the LR.

During the post-monsoon and winter, due to the absence of the monsoonal jet, moisture advection into the valley is strongly reduced due to the absence of the monsoonal jet. MR at higher stations decreases to approximately 1.0 $\mathrm{g\,kg^{-1}}$ and RH drops to 28 % in December. Consequently, LRs steepen and SW/LW ratios increase again, initiating strong surface heating and nocturnal radiative cooling that also characterizes the pre-monsoon.

4.1.2 Valley circulation

During the pre-monsoon, the strong surface heating and steep LR drive a pronounced diurnal mountain-valley wind regime, with anabatic winds during the day and cold, katabatic winds at night (Fig. 4). Anabatic winds peak during this season, where mean hourly wind speeds of 7 $\mathrm{m\,s^{-1}}$ are observed during the pre-monsoon between 12:00–14:00 at PLU1 (Fig. 4f). A comparable diurnal pattern persists through winter and the post-monsoon, though nocturnal and early-morning katabatic winds strengthen considerably during these seasons, particularly at PLU2 (5 $\mathrm{m\,s^{-1}}$) and PLU3 (3 $\mathrm{m\,s^{-1}}$) (Fig. 4b). This intensification is likely attributable to the presence of snow cover at the higher elevations of the catchment (Fig. B1), resulting in strong nocturnal radiative cooling that strengthen the density driven katabatic winds at these sites. At the onset of the monsoon, reduced surface heating and shallower lapse rates reduce along-valley temperature gradients (Fig. 3). As a result, the valley circulation abruptly weakens at the onset of the monsoon, indicated by the low wind speeds measured at each station. In July and August, the south-westerly directed monsoonal flow dominates the prevailing wind direction. As a result, the flow is directed upslope through most of the night for PLU3 and PLU1. At PLU2, the relative occurrence of katabatic winds increase, which could be due to its proximity to the ice body of Yala Glacier.

4.1.3 Precipitation

Monthly precipitation within the Langtang Valley exhibits high spatial heterogeneity and a pronounced seasonal cycle (Fig. 5a). The monsoon accounts for 60–70 % of the annual total, followed by the pre-monsoon (20–30 %). The post-monsoon and winter are substantially drier, together contributing less than 20 % of the annual total. Peak monthly precipitation consistently occurs in July throughout the valley, ranging from 148 mm at TB9 to 582 mm at TB2. Winter precipitation is characterized by high inter-annual variability as the wet day frequency is low and the amount is controlled by the magnitude of isolated events. During the monsoon, the highest precipitation totals are observed in the lower valley measuring 353 mm at TB1 and 582 mm at TB2 in July. At Kyangjin Village, a sharp decline in absolute precipitation is measured (PLU1: 169 mm in July). However, substantially higher precipitation totals are measured at higher elevations on adjacent slopes near the village: Here TB3-–5 measure 181, 238 and 199 mm and PLU2 measures 271 mm. On the main valley floor further up-valley from Kyangjin Village,

https://doi.org/10.5194/egusphere-2026-5005
Preprint. Discussion started: 2 September 2026

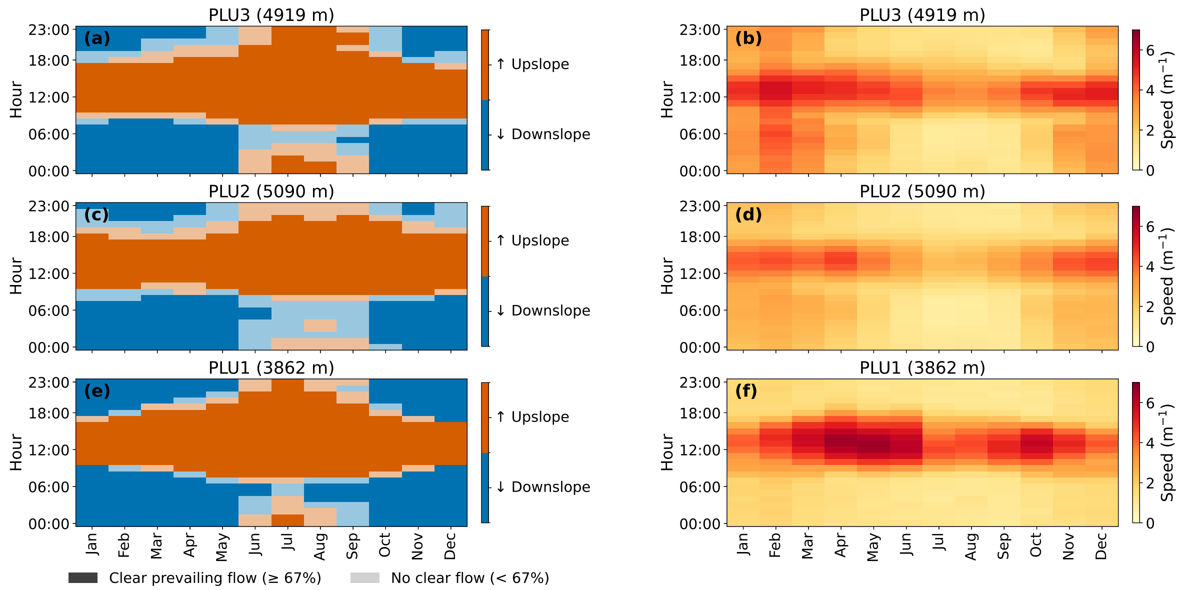

Figure 4. Prevailing hourly wind direction (upslope/downslope) per month (a, c, e) and mean hourly wind speed per month (b, d, f) for PLU3, PLU2 and PLU1. Color shading in the wind direction panels denotes the relative occurrence of each wind direction (dark: $\geq 67\,\%$ of the time; light: $< 67\,\%$).

precipitation totals are relatively constant for TB6, TB7 and TB9, which measure 158, 190, 148 mm in July, respectively. At PLU3, located inside the tributary valley of Morimoto glacier, a slightly higher monthly total (208 mm) is observed.

During the pre-monsoon a stronger decrease in precipitation up-valley is measured. Monthly precipitation totals measured at PLU1, TB3–5 and PLU2 are consistently higher relative to TB7, TB6, TB9, TB8 and PLU4 (Fig. 5). This drying up-valley trend suggests moisture depletion as air masses move further into the catchment. A near constant influx of moisture during the monsoon results in a high wet day frequency, but generally with small rainfall intensities (Fig. 5b). The wet day frequency during post-monsoon and winter is low, but the daily amounts can be considerable. Some of the most extreme daily totals are recorded during the monsoon–post-monsoon transition (e.g. the cyclone events Phailin, Hudhud, Hamoon and Yaas) (Fig. 5d). Snowfall at Kyangjin occurs primarily between November and April. In winter, snowfall mainly accumulates around Kyangjin and its surroundings up to PLU2. Extreme snowfall events are recorded at the end of the post-monsoon and during the winter. Overall, the highest snowfall amounts are observed between 12:00 and 14:00 at PLU1 as moisture availability is high compared to the winter and post-monsoon, while temperatures are considerably lower compared to the monsoon (Fig. 3d). At the end of the monsoon and at the start of the post-monsoon, a substantial part of the annual snowfall falls above 4900 m a.s.l. At Kyangjin, no persistent snow layer forms during the year, whereas higher sites like PLU2 remain snow covered until May (Fig. B1).

https://doi.org/10.5194/egusphere-2026-5005
Preprint. Discussion started: 2 September 2026

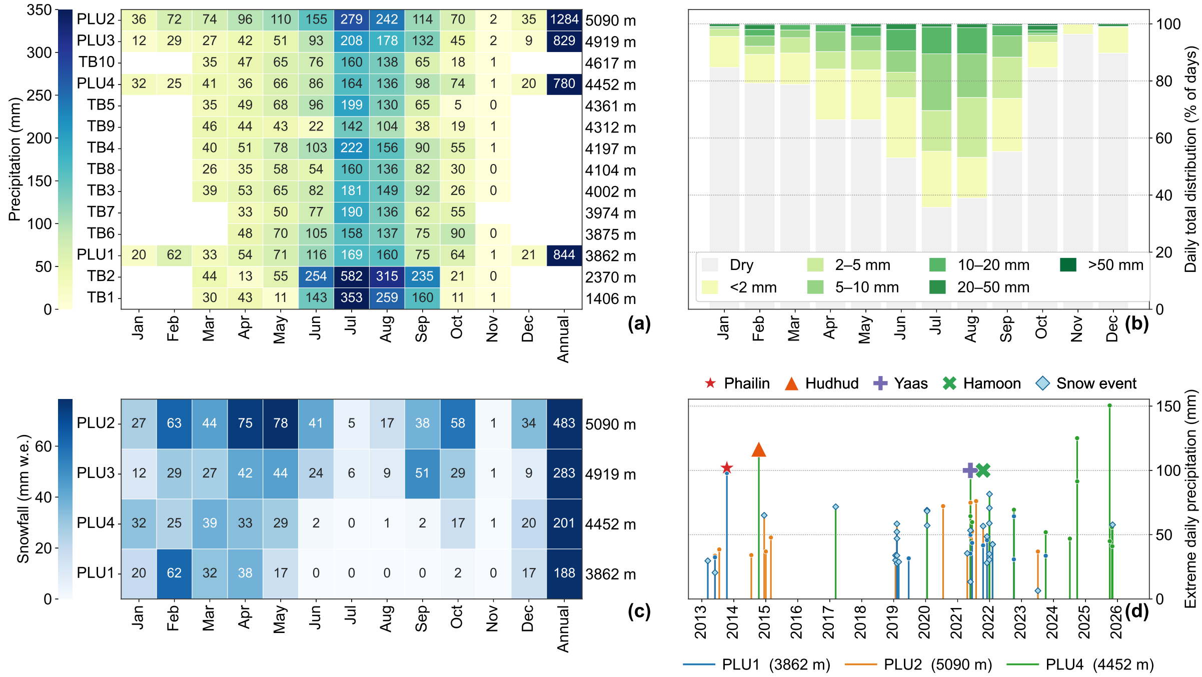

Figure 5. (a) Mean monthly precipitation (mm) for each station and annual totals for each pluviometer. (b) Mean monthly distribution of daily precipitation totals at PLU1 (3862 m a.s.l.). (c) Mean monthly snowfall (mm w.e.) measured at the pluviometers. (d) Top 20 extreme daily events for PLU1, PLU2 and PLU4 ($\mathrm{mm\,day^{-1}}$); snow events and well-known extreme events are indicated by markers.

4.2 Diurnal setting

4.2.1 Monsoon

285 During the monsoon, precipitation follows a clear diurnal cycle that is driven by weak valley winds (Fig. 6, Fig. 4). The characteristics of the diurnal precipitation cycle vary with elevation. At lower elevations (TB1 and TB2), a single nocturnal peak is observed (00:00–01:00), while at higher elevations (PLU1 and above), a bimodal pattern emerges with both an afternoon (13:00-14:00) and a nocturnal maximum (00:00-01:00) (Fig. 6, Fig. B2b). Throughout the day, surface heating destabilizes the lower boundary layer, LR slightly steepens, generating anabatic winds that peak at 14:00 (Fig. 4). Moisture advected into the 290 valley by the monsoonal jet is forced upslope by anabatic winds. During this period, maximum temperatures are measured (+11 °C above 5000 m a.s.l. at PLU2). Afternoon surface heating drives convective-type precipitation. This results in localized afternoon showers, indicated by the lower correlation in the precipitation signal between stations (Fig. B2a). At night, incoming solar radiation decreases, anabatic winds weaken, the air cools, and the cloud base lowers towards the valley floor. Meanwhile, continued monsoonal flow sustains high MR (e.g. 11 $\mathrm{g\,kg^{-1}}$ at PLU1) throughout the valley (Fig. 6c4). The combination of

https://doi.org/10.5194/egusphere-2026-5005
Preprint. Discussion started: 2 September 2026

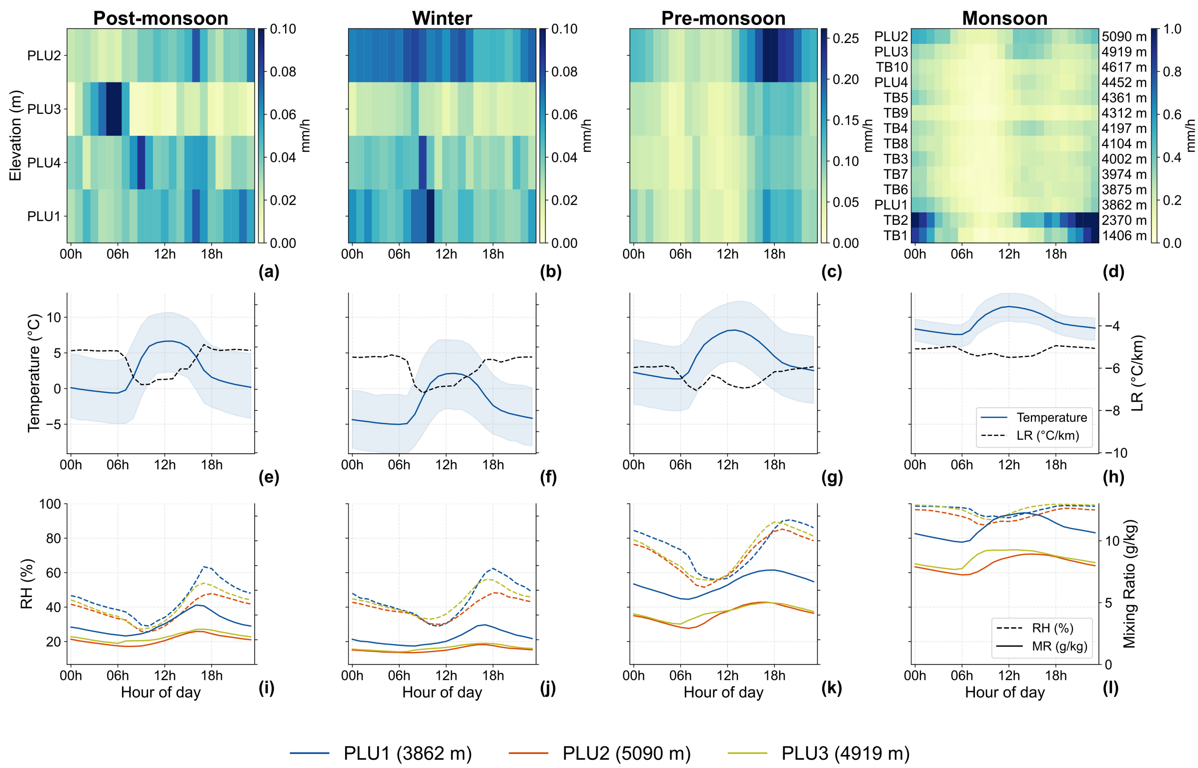

Figure 6. Mean hourly (a-d) precipitation, (e-h) LR and temperature (at PLU1), blue shading indicates the 10th to 90th percentile range of the hourly LR and (i-l) mixing ratio and relative humidity, per season (columns: post-monsoon, winter, pre-monsoon, monsoon).

high MR and radiative cooling results in a nearly saturated atmosphere, indicated by RH values approaching 100 % leading to the nocturnal precipitation peak.

From 02:00 to 03:00 onward, further cooling results in katabatic winds dominating across the valley until 07:00 (Fig. 4). The descent of colder, drier air associated with these katabatic flows subsequently suppresses precipitation to a minimum at 07:00–08:00.

To quantify how the shape of the diurnal monsoon precipitation cycle evolves with elevation, the afternoon (13:00–16:00) and nocturnal (21:00–00:00) peaks are compared across the elevational range using the normalized precipitation $\hat{p}$ (Eq. 2) (Fig. 7). A linear increase (decrease) of the relative amplitude of the afternoon (nocturnal) peak with elevation is indicated in Fig. 7a. At elevations below 3400 m a.s.l., the afternoon peak remains below the daily hourly mean (normalized value <1) and can be considered effectively absent, while the nocturnal peak is projected to fall below this mean only at altitudes above 5700 m a.s.l. The hourly elevation-precipitation gradient (slopes of the trendlines of Fig. 7a) shows that the gradient switches from positive during morning and afternoon hours to negative from 17:00 onwards (Fig. 7b).

https://doi.org/10.5194/egusphere-2026-5005
Preprint. Discussion started: 2 September 2026

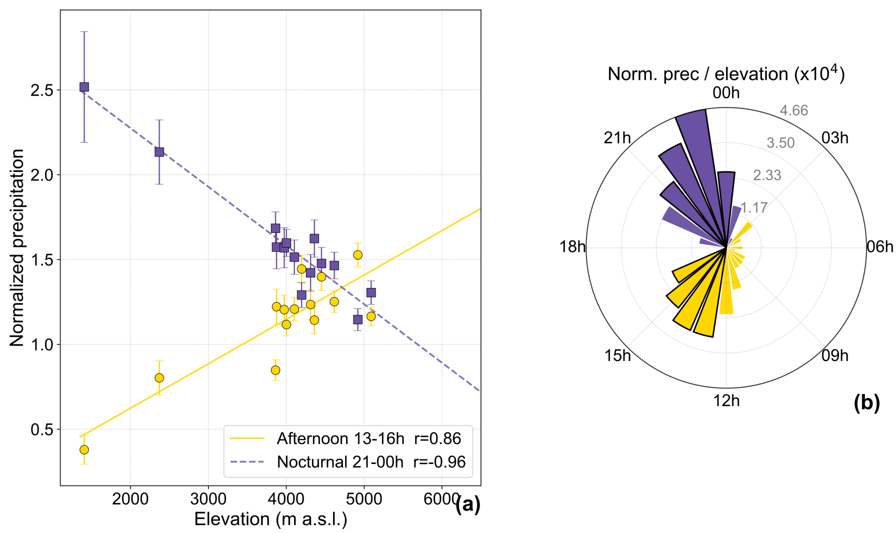

Figure 7. (a) Normalized precipitation at the selected daytime peak hour (13:00–16:00; yellow circles) and nocturnal peak hour (21:00–00:00; purple squares), plotted as a function of elevation. Error bars denote ± 1 standard error of the mean across monsoon days. Solid and dashed trendlines show least-squares fits for the daytime and nocturnal estimates, respectively. (b) Hourly regression slope of normalized precipitation values against elevation (slope of trendlines of panel a). Yellow bars indicate precipitation increasing with elevation (positive gradient, present in the afternoon) and purple bars indicate a negative gradient (present during nighttime). Normalized diurnal timeseries for PLU4 and TB2 are also provided in Fig. B2.

4.2.2 Pre-monsoon

In contrast to the bimodal precipitation pattern observed during the monsoon, the pre-monsoon period is generally characterized by a single daytime precipitation peak around 18:00 (Fig. 6), driven by localized convection resulting from intense surface heating and strong anabatic winds. At 18:00, convective precipitation is most pronounced at PLU1 and PLU2, with progressively smaller amounts recorded further valley inward at PLU3 and PLU4. The MR peak occurs approximately at 17:00. Following the afternoon precipitation maximum, rapid nocturnal radiative cooling increases the strength of katabatic winds across the valley (Fig. 4), suppressing further precipitation. Katabatic winds persist until 06:00–09:00 in the morning (Fig. 4) during which precipitation is minimal.

4.2.3 Winter and post-monsoon

During winter and the post-monsoon, MR and RH in the valley are considerably lower compared to the (pre-)monsoon, ranging between 2–4 $\mathrm{g\,kg^{-1}}$ and (20–40 %), respectively. Nocturnal LR vary between -5.5 and -5 $^{\circ}\mathrm{C\,km^{-1}}$, steepening to -6.5 to $-7.0\,^{\circ}\mathrm{C\,km^{-1}}$ during daytime. MR peaks at 16:00 reaching 4 $\mathrm{g\,kg^{-1}}$ during the post-monsoon and 3.2 $\mathrm{g\,kg^{-1}}$ during the winter at PLU1. Similar MR values at PLU2 and PLU3 indicate a spatially uniform moisture distribution across the valley

https://doi.org/10.5194/egusphere-2026-5005
Preprint. Discussion started: 2 September 2026

during these seasons. Although a strong valley wind circulation exists, under these dry conditions, no statistically significant diurnal precipitation cycle or vertical precipitation gradient is detected.

5 Discussion

5.1 Spatial precipitation patterns

Observations from this study demonstrate that precipitation in the Langtang Valley is highly heterogeneous in both space and time. This variability implies that validation of regional climate models or satellite products against individual station measurements should be treated with caution, as single stations are unlikely to be representative for a catchment as a whole. This is especially true during the (pre-)monsoon, where it is mainly local convection, rather than synoptic forcing, that governs the spatial distribution of precipitation. Despite this heterogeneity, precipitation totals along the main valley floor correspond reasonably well with regional elevation-precipitation trends. The observed precipitation maximum at TB2 (2370 m a.s.l.; Fig. 8) during the monsoon, which shifts to 3000–4000 m a.s.l. during the pre-monsoon, is broadly consistent with regional WRF simulations from Karki et al. (2017). This correspondence breaks down at Yala (PLU2). The anomalously high precipitation totals recorded at PLU2, situated near the tongue of Yala Glacier, are related to enhanced local convergence driven by glacial surface cooling (Potter et al., 2018; Lin et al., 2021). Here upslope flows in combination with an increased presence of katabatic winds (Fig. 4c) lead to local convergence zones, that can result in a local precipitation maximum at the front the of the glacier. We therefore caution against applying regional elevation-precipitation relations (Sugimoto and Takahashi, 2016; Bookhagen and Burbank, 2006) for sites located near glaciers.

The observed transition from a single nocturnal peak to a bimodal diurnal cycle above 3400 m a.s.l. confirms regional observations and modeling studies (Fujinami et al., 2025; Barros et al., 2000, 2004; Shea et al., 2015; Fujinami et al., 2021). Based on observed ground data, we extend this research by showing that the amplitude of the monsoon precipitation peaks varies linearly with elevation (Fig. 7). Normalization (Eq. 2) removes the local controls on precipitation totals, isolating the relative importance of the processes that govern the diurnal cycle: thermally driven daytime convection that strengthens with elevation (afternoon) and the orographic lifting of the monsoonal jet (nocturnal, Sect. 5.3). We therefore argue that the empirically derived relation in Fig. 7 offers a quantitative tool for model evaluation. A model that reproduces the linear increase (decrease) of the afternoon (nocturnal) peak with elevation captures the essential monsoon dynamics of the valley. Further research could test the transferability of this relation to other valleys in the Himalayas as well as other monsoon dominated mountain regions, such as the Andes, where a twice daily maximum occurs with similar altitudinal trends as in the Himalayas (Junquas et al., 2018). To better understand what mechanisms drive these peaks, the following sections examine why the nocturnal peak dominates the monsoon profile (Sect. 5.2), and how this topographic sensitivity changes across other seasons (Sect. 5.3).

https://doi.org/10.5194/egusphere-2026-5005
Preprint. Discussion started: 2 September 2026

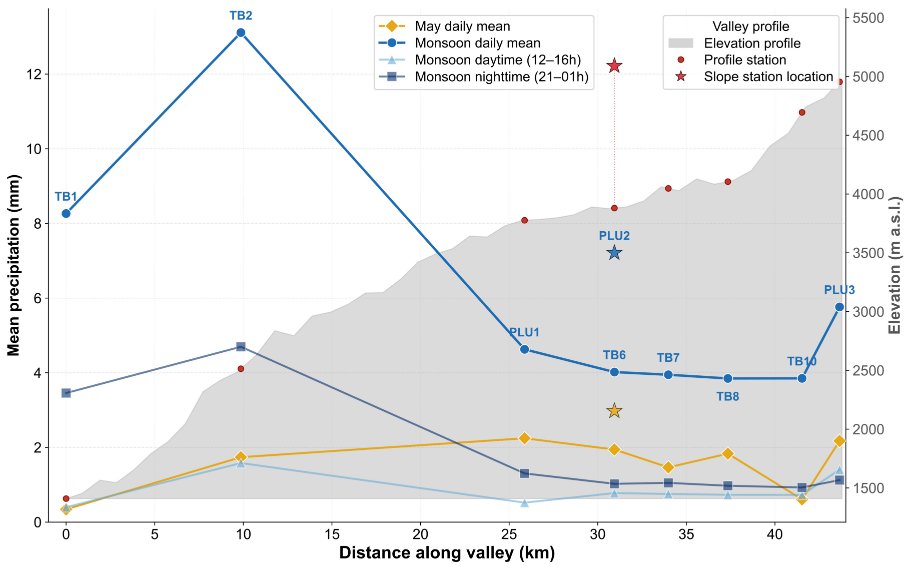

Figure 8. Mean daily monsoon precipitation (blue), mean monsoon nocturnal/afternoon precipitation (dark/light blue) , mean daily pre-monsoon (May) precipitation (yellow), along the valley floor profile (grey). Star marker depict mean daily monsoon precipitation measured at PLU2.

5.2 Monsoon nocturnal precipitation

While the afternoon peak is relatively more pronounced at high altitudes, its absolute precipitation contribution is insufficient to offset the large nocturnal totals concentrated at valley entrances and lower slopes (Fig. 8). It is therefore the nocturnal peak that ultimately determines the overall trends of the precipitation-elevation profile during the monsoon. On a synoptic scale, Fujinami et al. (2021, 2022) argue that nocturnal peaks in the Himalayas can partly be attributed to the acceleration of the low-level monsoon flow over the Gangetic Plain. This acceleration maximizes moisture transport toward the Himalayan foothills between midnight and early morning. Barros and Lang (2003) state that nocturnal wind speeds decrease or even reverse near the mountain barrier. As a result, the near-surface winds converge, leading to upward motion that can force convection. At the valley scale, Barros et al. (2004) argue that nocturnal cooling, in combination with a steady daytime buildup of precipitable water, drives this nocturnal maximum. This process is further aided by evaporative cooling from rainfall early in the night and moisture input from evapotranspiration below 3000 m a.s.l. Cloud-resolving WRF simulations suggest that katabatic winds, driven by nighttime radiative cooling and evaporative cooling by hydrometeors in the near-surface layer, converge with the monsoonal jet to produce the nocturnal precipitation peak (Sugimoto et al., 2021). The nocturnal maximum observed in the Andes has likewise been attributed to convergence of katabatic winds with the monsoonal flow (Junquas et al., 2018). Although we tested the relationship between downslope wind speed and precipitation intensity across all stations, a significant positive correlation was found only near the front of Yala Glacier at PLU2, indicating a local convergence zone

https://doi.org/10.5194/egusphere-2026-5005
Preprint. Discussion started: 2 September 2026

that does not extend to Kyangjin Village (PLU1). Additional wind measurements in the lower valley are needed to study how the interaction between katabatic winds and the monsoonal jet results in a nocturnal precipitation peak below 3000 m a.s.l. In addition to these processes, we hypothesize that the nocturnal maximum in precipitation below 3000 m a.s.l. in the Langtang Valley is also a result of the steep, confined valley geometry found here (Fig. 1b). Radiative cooling in combination with high MR brings the atmosphere towards saturation (RH ∼100 %) during nighttime (Fig. 6c). Under these near-saturated conditions, the lifting condensation level lies close to the surface and lifted air ascends along the moist adiabat. Because the LR is close to the moist-adiabatic lapse rate, this ascent is neither inhibited nor buoyantly accelerated. The shallow monsoon LR, although stable for unsaturated air, offers little resistance to saturated ascent (Kirshbaum et al., 2018), allowing the monsoonal flow to be lifted over the terrain. Under these conditions the rate at which moist air is mechanically lifted and cooled is proportional to the slope, and under fully saturated conditions the condensation rate can be approximated using the formulation from Colton (1976)

$$C(x,y) = \rho\, q_{\mathrm{VSAT0}} \boldsymbol{U} \cdot \nabla h(x,y), \tag{3}$$

where ρ the air density and q_{VSAT0} the saturation specific humidity at the ground, which depends on temperature (T, in °C) according to $q_{\mathrm{VSAT0}} \approx 0.0038\exp(0.068T)$. The second term, $\boldsymbol{U} \cdot \nabla h(x,y)$, represents the terrain-forced ascent, where $\boldsymbol{U}$ is the mean wind vector and $\nabla h(x,y)$ the terrain slope. The relatively warm temperatures and high moisture availability in combination with sustained nocturnal upslope flow results in high values for q_{VSAT0}. As a result, variation in $\boldsymbol{U} \circ \nabla h(x,y)$ strongly modulate condensation rates. Figure 8 illustrates this, where the steep valley bottom and surrounding slopes at TB1 and TB2 (Fig. 1) result in a peak in the nocturnal precipitation. This may explain why a sudden drop in precipitation is found between TB2 and PLU1, as between these stations, the valley widens and the slope flattens. The position of such slope breaks along Himalayan valleys is largely set by the extent of glaciers during the Last Glacial Maximum and by region-wide tectonics, and may therefore occur at comparable elevations across the region (Owen, 2020; Schmidt et al., 2015; Kashyap et al., 2024). This suggests that the regional precipitation-elevation pattern during the monsoon may partly be attributed to this shared valley morphology. Future studies could test whether sudden decreases in precipitation in other Himalayan valleys coincide with this morphological transition.

5.3 Seasonal shifts in precipitation-topography interaction

The sensitivity of precipitation to valley topography is strongly modulated by atmospheric moisture availability. In the pre-monsoon, the strongest valley circulation is measured (Fig. 4). Still, the terrain forced ascent mechanism (Eq. 3) does not apply as limited moisture availability results in an unsaturated atmosphere. During this period, moisture generally originates from regional evapotranspiration in contrast to the large scale moisture influx during the monsoon (Barros and Lang, 2003). Due to the lower atmospheric moisture content, further cooling (or lifting) is needed for condensation (Fig. 9). As a result, the peak in precipitation at TB2 is absent, indicating that the terrain term exerts limited control on the precipitation totals (Fig. 8). During winter and post-monsoon, moisture resides primarily in the upper atmosphere, and valley geometry and local

https://doi.org/10.5194/egusphere-2026-5005
Preprint. Discussion started: 2 September 2026

temperature fluctuations exert minimal influence on the precipitation distribution. During this period, synoptic-scale weather systems govern precipitation patterns.

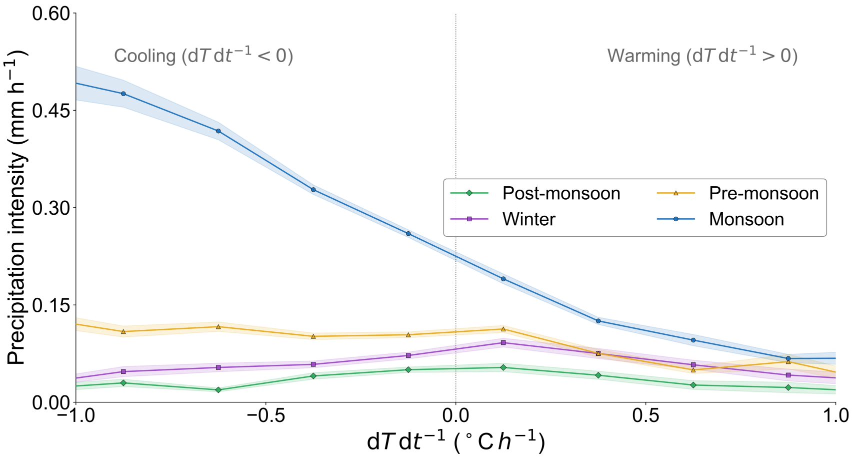

Figure 9. Seasonal precipitation sensitivity to cooling ($\mathrm{d}T/\mathrm{d}t < 0$) and warming ($\mathrm{d}T/\mathrm{d}t > 0$). Hourly temperature changes are binned every 0.1 °C, and the mean precipitation intensity for each bin is indicated on the y-axis. Shaded areas indicate ± 1 standard error of the mean across all hourly observations within each temperature-change bin.

6 Conclusions

During the monsoon, the spatial distribution of precipitation is primarily controlled by valley topography and the diurnal valley circulation. Above approximately 3400 m a.s.l., a bimodal precipitation pattern emerges, comprising an afternoon maximum driven by convective activity and a nocturnal maximum sustained by radiative cooling and orographically forced ascent of moisture-laden air. At lower elevations, the steep and confined V-shaped valley geometry enhances orographic uplift and low-level convergence, concentrating the highest absolute precipitation totals near the valley entrance. The monsoon precipitation-elevation gradient reverses diurnally, shifting from positive during afternoon hours to negative at night. As the absolute contribution of the nocturnal peak consistently dominates that of the afternoon convective peak throughout the valley, it is the nocturnal maximum that ultimately determines the shape of the monsoon precipitation-elevation profile. During the pre-monsoon, the absence of large-scale moisture influx results in an unsaturated atmosphere where terrain-forced ascent exerts limited control. Instead, strong surface heating and steep lapse rates drive a pronounced valley circulation, producing a single afternoon convective precipitation peak that migrates upward along the valley during the day. In winter and the post-monsoon, synoptic-scale weather systems govern precipitation, and no statistically significant diurnal or vertical precipitation gradients are detected. Under the near-saturated atmospheric conditions prevailing during the monsoon, precipitation totals are sensitive to local topography and valley circulation strength. This sensitivity diminishes outside the monsoon, when the atmosphere is sufficiently unsaturated that additional cooling is required before precipitation is triggered. We provide a generalized gradi-

https://doi.org/10.5194/egusphere-2026-5005
Preprint. Discussion started: 2 September 2026

ent of the monsoonal cycle with elevation that can be used as validation to evaluate model performance in reproducing the elevation-dependent shift between afternoon and nocturnal precipitation peaks, which is a measure on how well models simulate the topography and the related valley circulation. The long-term observational record compiled here provides a unique reference dataset to support such model development and validation.

Code and data availability. The post-processed data described in this manuscript can be accessed at Zenodo under https://doi.org/10.5281/zenodo.21419293 (Kwadijk, 2026a) and will be publicly available after revision. Data are co-owned by ICIMOD, DHM (all setups), Utrecht University (all setups excl. SNOWAMP) and NVE (SNOWAMP stations). Raw data can be accessed via https://rds.icimod.org/metadata/search?q=langtang&page=1&per_page=9&qKeyword= or upon request: w.w.immerzeel@uu.nl. Further description and accessibility of the data is also provided in Steiner et al. (2021). Code for the post-processing and analysis performed in this study is available at Github under https://doi.org/10.5281/zenodo.22043096 (Kwadijk, 2026b).

Author contributions. Conceptualization: AK, WWI FMN. Methodology: AK. Formal analysis: AK. Investigation: AK. Data curation: AK, PDAK, JFS. Visualization: AK. Writing:-original draft: AK. Resources: PDAK, JMS, JFS, WWI. Supervision: FMN, WWI. Writing-review and editing: PDAK, FMN, JMS, JFS, WWI, RRW. Funding Acquisition: WWI. Project Administration: WWI

Competing interests. The authors declare that they have no conflict of interest.

Acknowledgements. We thank ICIMOD, ETH and DHM for their contributions in financing, installing and maintaining a part of the station network present in the Langtang Valley. Special thanks to Simon Wicki, Martin Heynen, Evan Miles and Eduardo Soteras for their efforts in the installation and maintenance of the Morimoto Pluvio (PLU3); to Bikas Bhattarai, Sharad Joshi, Rijan Kayastha, Niraj Pradhananga and Dorothea Stumm for the installation and maintenance of the Kyanging (PLU1), Yala (PLU2). AI was used in the generation of code and improvement of writing.

Financial support. This project has received funding from the European Research Council (ERC) under the European Union's Horizon Framework research and innovation program (grant agreement No 101142123; 'DROP' project) and by the the NWO Talent Programme Veni (grant agreement VI.Veni.222.019; 'GREENPEAKS' project) which is financed by the Dutch Research Council (NWO). Views and opinions expressed are however those of the author(s) only and do not necessarily reflect those of the European Union or Dutch research council. Neither granting authority can be held responsible for them.

https://doi.org/10.5194/egusphere-2026-5005
Preprint. Discussion started: 2 September 2026

Appendix A: Supplemental figures method

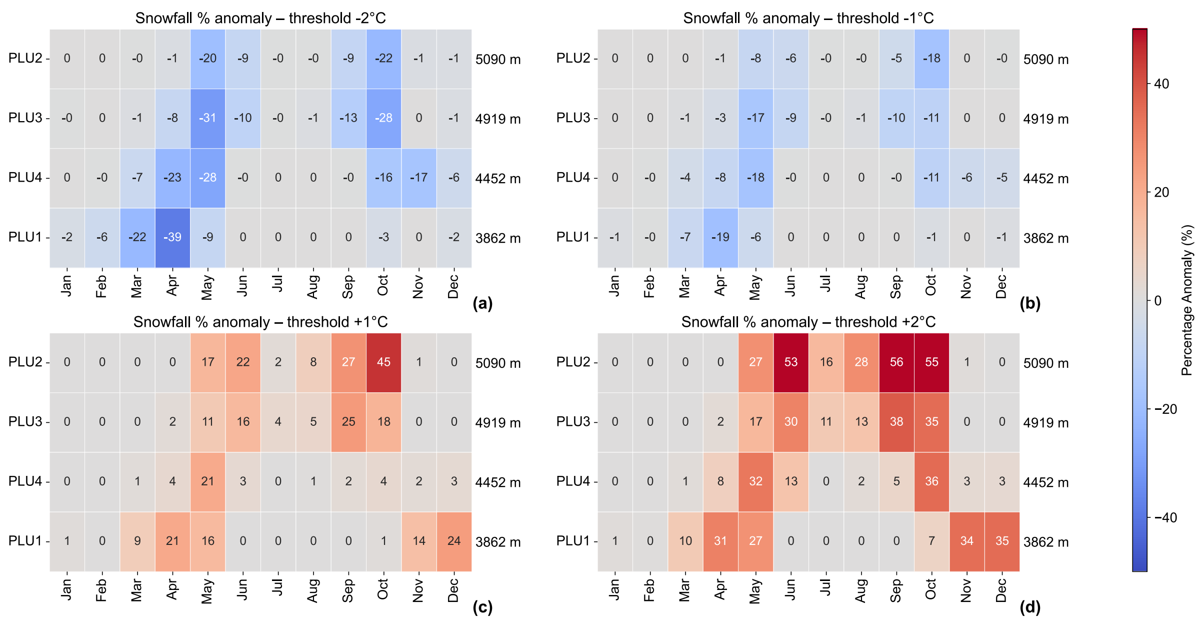

Figure A1. Snowfall anomaly (%) for different temperature thresholds relative to a temperature threshold of 0 °C.

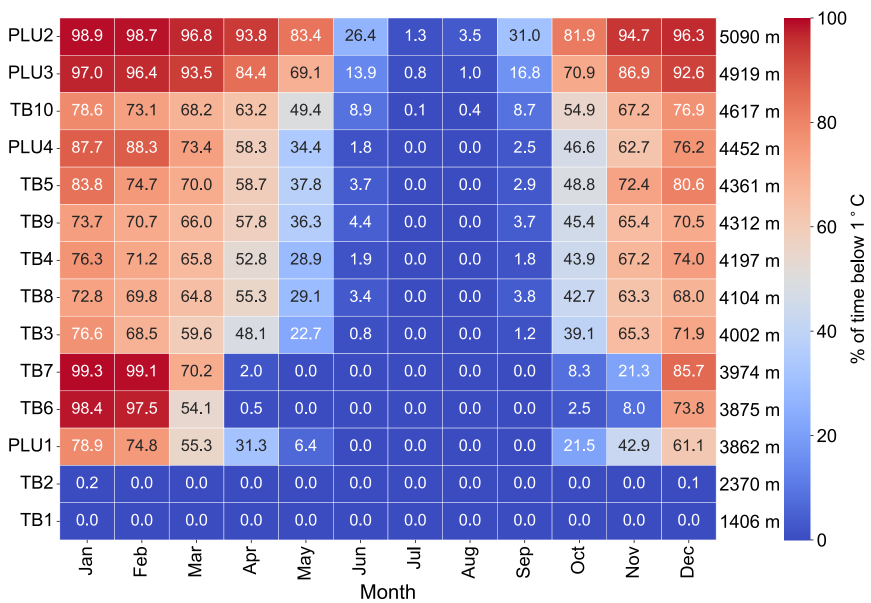

Figure A2. Percentage of time temperature is below snowfall temperature threshold of +1 °C for all tipping buckets and pluviometers.

https://doi.org/10.5194/egusphere-2026-5005
Preprint. Discussion started: 2 September 2026

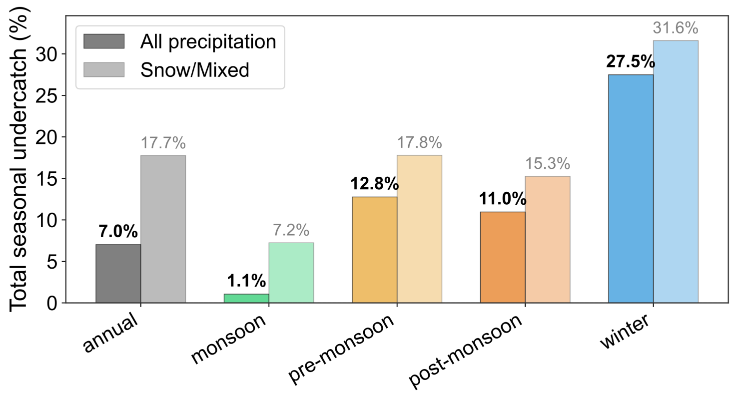

Figure A3. Seasonal estimated wind-induced undercatch from Kochendorfer et al. (2017) for the mixed and solid precipitation fraction at the combined precipitation totals of the pluviometers for total precipitation (snow + rain, dark shading) and solid/mixed only (light shading).

440 ## Appendix B: Supplemental figures results

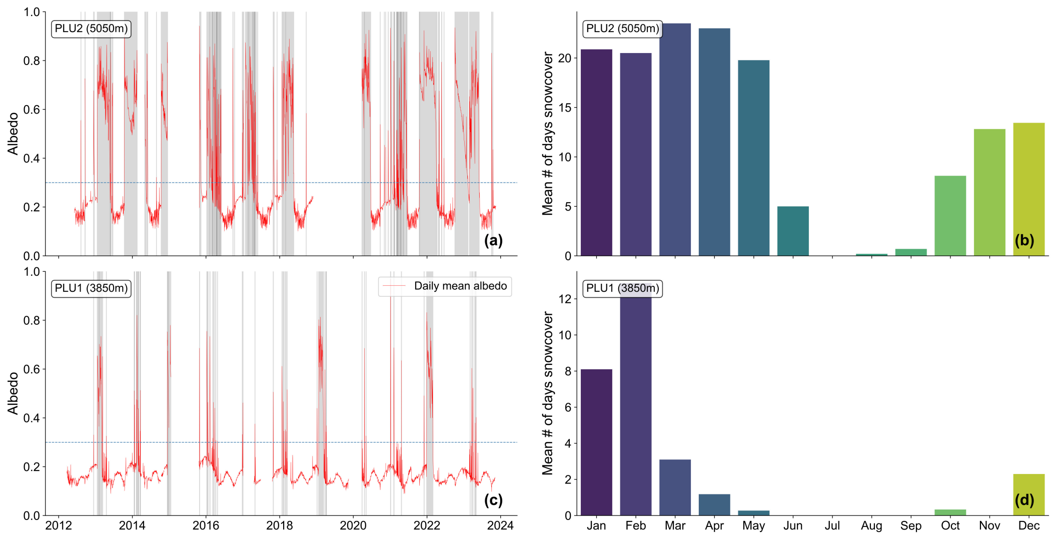

Figure B1. Albedo (SW_{out}/SW_{in}) timeseries for PLU2 (a) and PLU1 (c) and snow cover duration inside the valley defined as mean monthly percentage of time where $SW_{out}/SW_{in} > 0.3$ (right) for PLU2 (b) and PLU1 (d).

https://doi.org/10.5194/egusphere-2026-5005
Preprint. Discussion started: 2 September 2026

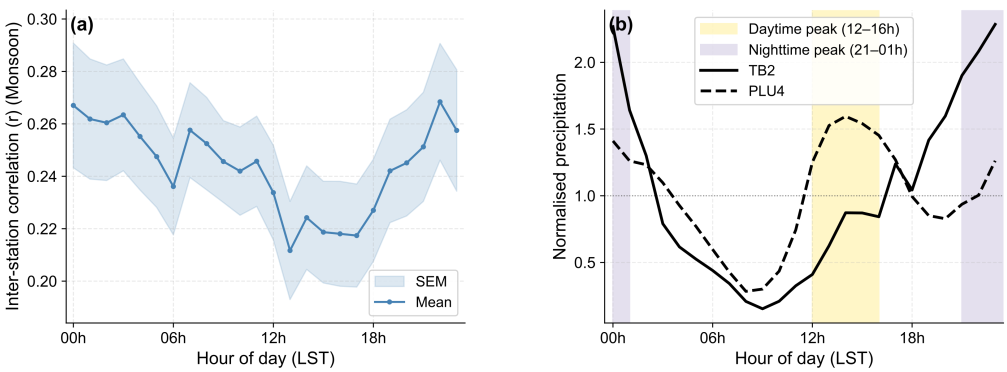

Figure B2. (a) Hourly mean Spearman correlation coefficient (r) between station pairs, calculated from coincident hourly precipitation measurements during the monsoon. Shading denotes ± 1 standard error of the mean across station-pair correlations for each hour of the day. (b) Normalized timeseries indicating the transition from a unimodal (nocturnal) precipitation peak (TB2, 2370 m a.s.l.) to a bimodal (afternoon and nocturnal) precipitation pattern (PLU4, 4919 m a.s.l)

https://doi.org/10.5194/egusphere-2026-5005
Preprint. Discussion started: 2 September 2026

References

Adhikari, S., Shrestha, D., Nepal, B., Chhetri, T. B., and Bhattarai, S.: Identification of Summer Monsoon Onset over Nepal by using Satellite-Derived OLR Data, Jalawaayu, 2, 19–32, https://doi.org/10.3126/jalawaayu.v2i1.45391, 2022.

Barros, A. P. and Lang, T. J.: Monitoring the Monsoon in the Himalayas: Observations in Central Nepal, June 2001, Monthly Weather Review, 131, 1408–1427, https://doi.org/10.1175/1520-0493(2003)131<1408:MTMITH>2.0.CO;2, 2003.

Barros, A. P., Joshi, M., Putkonen, J., and Burbank, D. W.: A study of 1999 monsoon rainfall in a mountainous region in central Nepal using TRMM products and rain gauge observations, Geophysical Research Letters, 27, 3683–3686, https://doi.org/10.1029/2000GL011827, 2000.

Barros, A. P., Kim, G., Williams, E., and Nesbitt, S. W.: Probing orographic controls in the Himalayas during the monsoon using satellite imagery, Natural Hazards and Earth System Sciences, 4, 29–51, https://doi.org/10.5194/nhess-4-29-2004, 2004.

Bharti, V. and Singh, C.: Evaluation of error in TRMM 3B42V7 precipitation estimates over the Himalayan region, Journal of Geophysical Research: Atmospheres, 120, 12 458–12 473, https://doi.org/10.1002/2015JD023779, _eprint: https://agupubs.onlinelibrary.wiley.com/doi/pdf/10.1002/2015JD023779, 2015.

Bhattacharya, A., Bolch, T., Mukherjee, K., King, O., Menounos, B., Kapitsa, V., Neckel, N., Yang, W., and Yao, T.: High Mountain Asian glacier response to climate revealed by multi-temporal satellite observations since the 1960s, Nature Communications, 12, 4133, https://doi.org/10.1038/s41467-021-24180-y, 2021.

Bolton, D.: The Computation of Equivalent Potential Temperature, Monthly Weather Review, 108, 1046 – 1053, https://doi.org/10.1175/1520-0493(1980)108<1046:TCOEPT>2.0.CO;2, 1980.

Bonekamp, P. N. J., Collier, E., and Immerzeel, W.: The Impact of Spatial Resolution, Land Use, and Spinup Time on Resolving Spatial Precipitation Patterns in the Himalayas, Journal of Hydrometeorology, 19, 1565–1581, https://doi.org/10.1175/JHM-D-17-0212.1, iSBN: 28.2108185.5, 2018.

Bookhagen, B. and Burbank, D. W.: Topography, relief, and TRMM-derived rainfall variations along the Himalaya, Geophysical Research Letters, 33, https://doi.org/10.1029/2006GL026037, _eprint: https://agupubs.onlinelibrary.wiley.com/doi/pdf/10.1029/2006GL026037, 2006.

Bookhagen, B. and Burbank, D. W.: Toward a complete Himalayan hydrological budget: Spatiotemporal distribution of snowmelt and rainfall and their impact on river discharge, Journal of Geophysical Research: Earth Surface, 115, 3019, https://doi.org/10.1029/2009JF001426, 2010.

Cannon, F., Carvalho, L. M. V., Jones, C., and Norris, J.: Winter westerly disturbance dynamics and precipitation in the western Himalaya and Karakoram: a wave-tracking approach, Theoretical and Applied Climatology, 125, 27–44, https://doi.org/10.1007/S00704-015-1489-8/TABLES/1, 2016.

Collier, E. and Immerzeel, W. W.: High-resolution modeling of atmospheric dynamics in the Nepalese Himalaya, Journal of Geophysical Research: Atmospheres, 120, 9882–9896, https://doi.org/10.1002/2015JD023266, 2015.

Colton, D. E.: Numerical Simulation of the Orographically Induced Precipitation Distribution for Use in Hydrologic Analysis, Journal of Applied Meteorology (1962-1982), 15, 1241–1251, http://www.jstor.org/stable/26177611, 1976.

de Kok, R. J., Kraaijenbrink, P. D. A., Tuinenburg, O. A., Bonekamp, P. N. J., and Immerzeel, W. W.: Towards understanding the pattern of glacier mass balances in High Mountain Asia using regional climatic modelling, The Cryosphere, 14, 3215–3234, https://doi.org/10.5194/tc-14-3215-2020, 2020.

EvK2CNR: EvK2CNR - Annual report 2025, Tech. rep., EvK2CNR, https://www.evk2cnr.org/en/p-e-p/annual-report, 2025.

Fujinami, H., Fujita, K., Takahashi, N., Sato, T., Kanamori, H., Sunako, S., and Kayastha, R. B.: Twice-Daily Monsoon Precipitation Maxima in the Himalayas Driven by Land Surface Effects, Journal of Geophysical Research: Atmospheres, 126, e2020JD034 255, https://doi.org/10.1029/2020JD034255, 2021.

Fujinami, H., Sato, T., Kanamori, H., and Kato, M.: Nocturnal Southerly Moist Surge Parallel to the Coastline Over the Western Bay of Bengal, Geophysical Research Letters, 49, e2022GL100 174, https://doi.org/10.1029/2022GL100174, 2022.

Fujinami, H., Sugimoto, S., Ueno, K., Fujinami, H., Sugimoto, S., Ueno, K., Das, S., and Tao, W.-K.: Dynamics of Rainstorms Over Southern Himalayan Slopes and Foothills and Their Simulation by Numerical Models, Severe Storms, pp. 333–359, https://doi.org/10.1007/978-981-97-7075-5_13, iSBN: 978-981-97-7075-5, 2025.

Gelsor, N., Juan, L., Wangmo, T., Tunzhup, L., and Gelsor, N.: Measurements on Solar Energy Resources in the Mt. Everest Region, American Journal of Physics and Applications, 9, 1–9, https://doi.org/10.11648/j.ajpa.20210901.11, 2021.

Hassenruck-Gudipati, H. J., Andermann, C., Dee, S., Brunello, C. F., Baidya, K. P., Sachse, D., Meyer, H., and Hovius, N.: Moisture Sources and Pathways Determine Stable Isotope Signature of Himalayan Waters in Nepal, AGU Advances, 4, e2022AV000 735, https://doi.org/10.1029/2022AV000735, _eprint: https://agupubs.onlinelibrary.wiley.com/doi/pdf/10.1029/2022AV000735, 2023.

Heynen, M., Miles, E., Ragettli, S., Buri, P., Immerzeel, W. W., and Pellicciotti, F.: Air temperature variability in a high-elevation Himalayan catchment, Annals of Glaciology, 57, 212–222, https://doi.org/10.3189/2016AoG71A076, 2016.

Immerzeel, W. W., Petersen, L., Ragettli, S., and Pellicciotti, F.: The importance of observed gradients of air temperature and precipitation for modeling runoff from a glacierized watershed in the Nepalese Himalayas, Water Resources Research, 50, 2212–2226, https://doi.org/10.1002/2013WR014506, 2014.

Immerzeel, W. W., Lutz, A. F., Andrade, M., Bahl, A., Biemans, H., Bolch, T., Hyde, S., Brumby, S., Davies, B. J., Elmore, A. C., Emmer, A., Feng, M., Fernández, A., Haritashya, U., Kargel, J. S., Koppes, M., Kraaijenbrink, P. D. A., Kulkarni, A. V., Mayewski, P. A., Nepal, S., Pacheco, P., Painter, T. H., Pellicciotti, F., Rajaram, H., Rupper, S., Sinisalo, A., Shrestha, A. B., Viviroli, D., Wada, Y., Xiao, C., Yao, T., and Baillie, J. E. M.: Importance and vulnerability of the world's water towers, Nature 2019 577:7790, 577, 364–369, https://doi.org/10.1038/s41586-019-1822-y, 2019.

Junquas, C., Takahashi, K., Condom, T., Espinoza, J.-C., Chavez, S., Sicart, J.-E., and Lebel, T.: Understanding the influence of orography on the precipitation diurnal cycle and the associated atmospheric processes in the central Andes, Climate Dynamics, 50, 3995–4017, https://doi.org/10.1007/s00382-017-3858-8, 2018.

Karki, R., Ul Hasson, S., Gerlitz, L., Schickhoff, U., Scholten, T., and Böhner, J.: Quantifying the added value of convection-permitting climate simulations in complex terrain: a systematic evaluation of WRF over the Himalayas, Earth System Dynamics, 8, 507–528, https://doi.org/10.5194/esd-8-507-2017, 2017.

Kashyap, A., Cook, K. L., and Behera, M. D.: Geomorphic evolution of Sutlej valley catchment in Western Himalayas: Imprint of surface processes in modulating fluvial erosion, Geomorphology, 465, 109 411, https://doi.org/10.1016/j.geomorph.2024.109411, 2024.

Khadka, A., Wagnon, P., Brun, F., Shrestha, D., Lejeune, Y., and Arnaud, Y.: Evaluation of ERA5-Land and HARv2 Reanalysis Data at High Elevation in the Upper Dudh Koshi Basin (Everest Region, Nepal), Journal of Applied Meteorology and Climatology, 61, 931–954, https://doi.org/10.1175/JAMC-D-21-0091.1, 2022.

Kirkham, J. D., Koch, I., Saloranta, T. M., Litt, M., Stigter, E. E., Møen, K., Thapa, A., Melvold, K., and Immerzeel, W. W.: Near Real-Time Measurement of Snow Water Equivalent in the Nepal Himalayas, Frontiers in Earth Science, 7, 177, https://doi.org/10.3389/feart.2019.00177, 2019.

https://doi.org/10.5194/egusphere-2026-5005
Preprint. Discussion started: 2 September 2026

Kirshbaum, D. J., Adler, B., Kalthoff, N., Barthlott, C., and Serafin, S.: Moist Orographic Convection: Physical Mechanisms and Links to Surface-Exchange Processes, Atmosphere, 9, 80, https://doi.org/10.3390/atmos9030080, 2018.

Kochendorfer, J., Nitu, R., Wolff, M., Mekis, E., Rasmussen, R., Baker, B., Earle, M. E., Reverdin, A., Wong, K., Smith, C. D., Yang, D., Roulet, Y.-A., Buisan, S., Laine, T., Lee, G., Luis, J., Aceituno, C., Alastrué, J., Isaksen, K., Meyers, T., Braekkan, R., Landolt, S., Jachcik, A., and Poikonen, A.: Analysis of single-Alter-shielded and unshielded measurements of mixed and solid precipitation from WMO-SPICE, Hydrol. Earth Syst. Sci, 21, 3525–3542, https://doi.org/10.5194/hess-21-3525-2017, 2017.

Kwadijk, A.: High altitude precipitation dynamics using long-term observations in a Himalayan catchment, Zenodo [data set], https://doi.org/10.5281/zenodo.21419293, 2026a.

Kwadijk, A.: Langtang precipitation, Github [repository], https://doi.org/10.5281/zenodo.22043097, 2026b.

Lin, C., Yang, K., Chen, D., Guyennon, N., Balestrini, R., Yang, X., Acharya, S., Ou, T., Yao, T., Tartari, G., and Salerno, F.: Summer afternoon precipitation associated with wind convergence near the Himalayan glacier fronts, Atmospheric Research, 259, 105 658, https://doi.org/10.1016/J.ATMOSRES.2021.105658, 2021.

Mal, S., Singh, R., and Huggel, C., eds.: Climate Change, Extreme Events and Disaster Risk Reduction: Towards Sustainable Development Goals, Sustainable Development Goals Series, Springer International Publishing, Cham, ISBN 978-3-319-56468-5 978-3-319-56469-2, https://doi.org/10.1007/978-3-319-56469-2, 2018.

Muñoz-Sabater, J., Dutra, E., Agustí-Panareda, A., Albergel, C., Arduini, G., Balsamo, G., Boussetta, S., Choulga, M., Harrigan, S., Hersbach, H., Martens, B., Miralles, D. G., Piles, M., Rodríguez-Fernández, N. J., Zsoter, E., Buontempo, C., and Thépaut, J.-N.: ERA5-Land: a state-of-the-art global reanalysis dataset for land applications, Earth System Science Data, 13, 4349–4383, https://doi.org/10.5194/essd-13-4349-2021, 2021.

Owen, L. A.: Quaternary Glaciation of the Himalaya and Adjacent Mountains, in: Himalayan Weather and Climate and their Impact on the Environment, edited by Dimri, A., Bookhagen, B., Stoffel, M., and Yasunari, T., pp. 239–260, Springer International Publishing, Cham, ISBN 978-3-030-29684-1, https://doi.org/10.1007/978-3-030-29684-1_13, 2020.

Pokhrel, P., Griffioen, J., Bogaard, T. A., Kraaijenbrink, P. D., Fiddes, J., and Immerzeel, W. W.: Upstream hydrology and the importance of snowmelt in buffering droughts in the Karnali basin in Nepal, Frontiers in Water, 7, https://doi.org/10.3389/frwa.2025.1720178, 2026.

Pollock, M. D., O'Donnell, G., Quinn, P., Dutton, M., Black, A., Wilkinson, M. E., Colli, M., Stagnaro, M., Lanza, L. G., Lewis, E., Kilsby, C. G., and O'Connell, P. E.: Quantifying and Mitigating Wind-Induced Undercatch in Rainfall Measurements, Water Resources Research, 54, 3863–3875, https://doi.org/10.1029/2017WR022421, 2018.

Potter, E. R., Orr, A., Willis, I. C., Bannister, D., and Salerno, F.: Dynamical Drivers of the Local Wind Regime in a Himalayan Valley, Journal of Geophysical Research: Atmospheres, 123, 13,186–13,202, https://doi.org/10.1029/2018JD029427, 2018.

Romshoo, S. A., Abdullah, T., Murtaza, K. O., and Bhat, M. H.: Direct, geodetic and simulated mass balance studies of the Kolahoi Glacier in the Kashmir Himalaya, India, Journal of Hydrology, 617, 129 019, https://doi.org/10.1016/j.jhydrol.2022.129019, 2023.

Salerno, F., Guyennon, N., Colombo, N., Melis, M. T., Dessì, F. G., Verza, G., Bista, K., Sheharyar, A., and Tartari, G.: What is climate change doing in the Himalaya? Thirty years of the Pyramid Meteorological Network (Nepal), Earth System Science Data, 17, 4293–4304, https://doi.org/10.5194/essd-17-4293-2025, 2025.

Saloranta, T., Thapa, A., Kirkham, J. D., Koch, I., Melvold, K., Stigter, E., Litt, M., and Møen, K.: A Model Setup for Mapping Snow Conditions in High-Mountain Himalaya, Frontiers in Earth Science, 7, https://doi.org/10.3389/feart.2019.00129, 2019.

https://doi.org/10.5194/egusphere-2026-5005
Preprint. Discussion started: 2 September 2026

Schmidt, J. L., Zeitler, P. K., Pazzaglia, F. J., Tremblay, M. M., Shuster, D. L., and Fox, M.: Knickpoint evolution on the Yarlung river: Evidence for late Cenozoic uplift of the southeastern Tibetan plateau margin, Earth and Planetary Science Letters, 430, 448–457, https://doi.org/10.1016/j.epsl.2015.08.041, 2015.

Shea, J., Wagnon, P., Immerzeel, W., Biron, R., Brun, F., and Pellicciotti, F.: A comparative high-altitude meteorological analysis from three catchments in the Nepalese Himalaya, International Journal of Water Resources Development, 31, 174–200, https://doi.org/10.1080/07900627.2015.1020417, 2015.

Steiner, J. F., Gurung, T. R., Joshi, S. P., Koch, I., Saloranta, T., Shea, J., Shrestha, A. B., Stigter, E., and Immerzeel, W. W.: Multi-year observations of the high mountain water cycle in the Langtang catchment, Central Himalaya, Hydrological Processes, 35, e14 189, https://doi.org/10.1002/HYP.14189, 2021.

Sugimoto, S. and Takahashi, H. G.: Effect of spatial resolution and cumulus parameterization on simulated precipitation over South Asia, Scientific Online Letters on the Atmosphere, 12, 7–12, https://doi.org/10.2151/sola.12A-002, 2016.

Sugimoto, S., Ueno, K., Fujinami, H., Nasuno, T., Sato, T., and Takahashi, H. G.: Cloud-Resolving-Model Simulations of Nocturnal Precipitation over the Himalayan Slopes and Foothills, Journal of Hydrometeorology, 22, 3171–3188, https://doi.org/10.1175/JHM-D-21-0103.1, 2021.

Tetens, O.: Uber einige meteorologische Begriffe, Z. geophys, 6, 297–309, 1930.

Ueno, K., Shiraiwa, T., and Yamada, T.: Precipitation Environment in the Langtang Valley, Nepal Himalayas, in: Snow and Glacier Hydrology (Proceedings of the Kathmandu Symposium, November 1992), edited by Young, G. J., no. 218 in IAHS Publication, pp. 207–219, IAHS Press, ISBN 0947571589, 1993.

Wang, L., Liu, H., Bhlon, R., Chen, D., Long, J., and Sherpa, T. C.: Modeling glacio-hydrological processes in the Himalayas: A review and future perspectives, Geography and Sustainability, 5, 179–192, https://doi.org/10.1016/j.geosus.2024.01.001, 2024.

Wang, X., Tolksdorf, V., Otto, M., and Scherer, D.: WRF-based dynamical downscaling of ERA5 reanalysis data for High Mountain Asia: Towards a new version of the High Asia Refined analysis, International Journal of Climatology, 41, 743–762, https://doi.org/10.1002/joc.6686, 2021.

Weidinger, J., Gerlitz, L., Bobrowski, M., Böhner, J., Chaudhary, R. P., Schickhoff, Udo, S., Schwab, N., and Scholten, T.: TREELINE - Longterm atmospheric and pedo-climatic observations along an upper treeline ecotone in the Himalayas, Nepal, https://doi.org/10.25592/uhhfdm.9563, 2021.

Whiteman, C. D. and Doran, J. C.: The Relationship between Overlying Synoptic-Scale Flows and Winds within a Valley, Journal of Applied Meteorology and Climatology, 32, 1669–1682, https://doi.org/10.1175/1520-0450(1993)032<1669:TRBOSS>2.0.CO;2, 1993.

Yang, K., Guyennon, N., Ouyang, L., Tian, L., Tartari, G., and Salerno, F.: Impact of summer monsoon on the elevation-dependence of meteorological variables in the south of central Himalaya, International Journal of Climatology, 38, 1748–1759, https://doi.org/10.1002/joc.5293, 2018.

Yoon, Y., Kumar, S. V., Forman, B. A., Zaitchik, B. F., Kwon, Y., Qian, Y., Rupper, S., Maggioni, V., Houser, P., Kirschbaum, D., Richey, A., Arendt, A., Mocko, D., Jacob, J., Bhanja, S., and Mukherjee, A.: Evaluating the uncertainty of terrestrial water budget components over high mountain Asia, Frontiers in Earth Science, 7, 449 754, https://doi.org/10.3389/FEART.2019.00120/BIBTEX, 2019.

Zhou, W., Peng, B., Shi, J., Wang, T., Dhital, Y., Yao, R., Yu, Y., Lei, Z., and Zhao, R.: Estimating High Resolution Daily Air Temperature Based on Remote Sensing Products and Climate Reanalysis Datasets over Glacierized Basins: A Case Study in the Langtang Valley, Nepal, Remote Sensing, 9, 959, https://doi.org/10.3390/rs9090959, 2017.